

Article

Numerical Study on the Formation Mechanism of Plume Bulge in the Pearl River Estuary under the Influence of River Discharge

Chenyu Zhao ^{1,2}, Nan Wang ^{1,2,*}, Yang Ding ^{1,3} , Dehai Song ^{1,3} , Junmin Li ⁴ , Mengqi Li ⁵ , Lingling Zhou ^{2,6}, Hang Yu ^{1,2}, Yanyu Chen ⁷ and Xianwen Bao ^{1,2,3}

¹ Frontier Science Center for Deep Ocean Multispheres and Earth System (FDOMES) and Physical Oceanography Laboratory, Ocean University of China, Qingdao 266100, China; chenyuzhao@stu.ouc.edu.cn (C.Z.); dingyangpol@ouc.edu.cn (Y.D.); songdh@ouc.edu.cn (D.S.); hangyu1008@stu.ouc.edu.cn (H.Y.); xwbao@ouc.edu.cn (X.B.)

² College of Oceanic and Atmospheric Sciences, Ocean University of China, Qingdao 266100, China; linglingzhou@ouc.edu.cn

³ Laoshan Laboratory, Qingdao 266237, China

⁴ South China Sea Institute of Oceanology, Guangzhou 510301, China; jli@scsio.ac.cn

⁵ Research Institute of Petroleum Exploration and Development, PetroChina, Beijing 100083, China; mengqili@petrochina.com.cn

⁶ Key Laboratory of Ocean Space Resource Management Technology, Ministry of Natural Resources, Hangzhou 310012, China

⁷ Marine Academy of Zhejiang Province, Hangzhou 310012, China; cyy@stu.ouc.edu.cn

* Correspondence: wangnan0515@ouc.edu.cn

Abstract: Previous studies have investigated the characteristics and influencing factors of plume bulge in the Pearl River Estuary (PRE) using observations and numerical simulations. However, the understanding of how river discharge affects plume bulge is not consistent, and the response mechanism of plume bulge to changes in river discharge has not been revealed in detail. In this study, a three-dimensional hydrodynamic Finite-Volume Coastal Ocean Model (FVCOM) is constructed, and five experiments were set to characterize the horizontal and vertical distribution of the plume bulge outside the PRE under different river discharge conditions during spring tide. The physical mechanisms of plume bulge generation and its response mechanisms to river discharge were discussed through standardized analysis and momentum diagnostic analysis. The results indicate that the plume bulge is sensitive to changes in river discharge. When the river discharge is relatively low (e.g., less than 11,720 m³/s observed in the dry season), the bulge cannot be formed. Conversely, when the river discharge is relatively high (e.g., exceeding 23,440 m³/s observed in flood season), the bulge is more significant. The plume bulge is formed by the anticyclonic flow resulting from the action of the Coriolis force on the strongly mixed river plume. The bulge remains stable under the combined effects of barotropic force, baroclinic gradient force, and Coriolis force. The reduction of river discharge weakens the mixing of freshwater and seawater, resulting in the reduction of both the volume and momentum of the river plume, and the balance between advective diffusion and Coriolis forces are altered, resulting in the plume, which is originally flushed out from the Lantau Channel, not being able to maintain the anticyclonic structure and instead floating out along the coast of the western side of the PRE, with the disappearance of the plume bulge. Due to the significant influence of plume bulges on the physical and biogeochemical interactions between estuaries and terrestrial environments, studying the physical mechanisms behind the formation of plume bulges is crucial.

Keywords: Pearl River Estuary; river plume bulge; FVCOM; river discharge; momentum balance analysis



Citation: Zhao, C.; Wang, N.; Ding, Y.; Song, D.; Li, J.; Li, M.; Zhou, L.; Yu, H.; Chen, Y.; Bao, X. Numerical Study on the Formation Mechanism of Plume Bulge in the Pearl River Estuary under the Influence of River Discharge. *Water* **2024**, *16*, 1296. <https://doi.org/10.3390/w16091296>

Academic Editor: Bommanna Krishnappan

Received: 7 April 2024

Revised: 25 April 2024

Accepted: 25 April 2024

Published: 2 May 2024



Copyright: © 2024 by the authors. Licensee MDPI, Basel, Switzerland. This article is an open access article distributed under the terms and conditions of the Creative Commons Attribution (CC BY) license (<https://creativecommons.org/licenses/by/4.0/>).

1. Introduction

Estuarine plume is formed by the mixing of freshwater from land into estuaries with seawater. Due to its lower salinity, it floats above the higher salinity seawater, spreading

out over the sea surface in a plume-like pattern [1]. It is generally believed that the plume of an estuary can be divided into four parts: the source region, the near-field, the mid-field, and the far-field. The dominant dynamical balance differs among each of these regions [1,2]. The formation of plumes in the source region depends on estuarine processes. In the Northern Hemisphere, if the width of the estuary is wider than the Rossby radius [1], the seawater flowing out from the source region will deflect to the right under the influence of the Coriolis force, forming coastal currents and moving in the direction of Kelvin wave [3,4]. Upon reaching the continental shelf, it flows along the shelf's isobaths and gradually dissipates as it mixes with the higher salinity seawater. The near field region begins at the river mouth and ends where the flow ceases to be supercritical ($Fr = 1$) [5,6]. The momentum balance in the near-field region is dominated by barotropic and baroclinic pressure gradients, turbulent interfacial stress, and flow acceleration [7]. River water transitions from a near-field jet into a geostrophic or wind-dominated far-field plume in the mid-field region. The dynamics of the plume in this region are increasingly dominated by the rotation of the Earth. Far-field may extend hundreds of kilometers from the river mouth, and the dynamics in this region are dominated by Earth's rotation, wind stress, and some bottom stress [1].

Plume dynamics govern the mixing of the plume with surrounding nearshore waters, influencing nutrient supply, phytoplankton growth rates, and cross-shelf transport [8–10]. Plumes also significantly affect hypoxic conditions in estuaries, as well as the physical and biogeochemical interactions between estuaries and terrestrial environments. The combination of nutrients provided by coastal upwellings and trace elements from plumes facilitates the formation of eutrophic zones in coastal areas [11,12]. Plume bulges, unstable anticyclonic eddies formed under specific conditions in the mid-field area, are prevalent in major estuaries worldwide, such as the Niagara River Estuary [13], the Hudson River Estuary [14], the Columbia River Estuary [15,16], and the Yangtze River Estuary [17], among others. However, plume bulge has not been observed in some estuaries, including Delaware Bay and Rhine outflows [18,19]. Therefore, the physical mechanisms behind the formation of estuarine plume bulges have become an important research topic.

Previous studies based on observations, laboratory experiments, and numerical models have extensively researched the formation mechanisms of plume bulges. It is considered that an estuarine plume bulge can form when the curvature radius of the freshwater at the estuary outlet is smaller than the inertial radius (the ratio of water flow velocity to the Coriolis force parameter) [9]. The Kelvin number (defined as the ratio of the estuary mouth's width to the baroclinic Rossby deformation radius) and fractional depth (defined as the ratio of the buoyancy layer depth to the surrounding ocean depth) were used to determine whether an estuarine plume bulge will form [20]. The conclusion is that a plume bulge is more likely to form in estuaries with low Kelvin numbers and fractional depth. If the Kelvin number and fractional depth at the estuary are high, the bottom friction will be increased due to the dynamic separation of inflowing and outflowing seawater, which disrupts the supercritical state of the flow and makes it difficult for the formation of the plume bulge.

Furthermore, estuary topography, wind, tides, and river discharge have all been shown to impact estuarine plume bulges. The depth of the Lantau Channel (LC) in Pearl River Estuary (PRE) is 20–30 m, and it is a fundamental factor in the formation of the plume bulge in PRE [21]. The effect of the wind produces different effects on the plume bulge depending on the location of the estuary and the direction of the wind [22–24]. Tidal dynamics is also a factor influencing the effect of the formation of plume bulges. During strong ebbing tides, intense advection promotes the appearance of a supercritical plume front, and the ebbing tide currents provide a significant influx of freshwater, making the bulge structure more stable [25,26]. Among these influencing factors, river discharge is generally considered the important driving factor of plume bulge formation [14,27]. The Finite-Volume Coastal Ocean Model (FVCOM) has been used to study the plume formation mechanism in the Chesapeake Bay, indicating that the volume of river discharge which

lags by one month is the primary cause of changes in plume area [28]. However, due to the unique dynamic environmental conditions of each estuary, the response of plume bulge to these factors varies.

The PRE, located in the northern part of the South China Sea (SCS), is China's second-largest river with strong river-sea interactions. The estuary shoreline forms a trumpet shape, narrowing in the north (about 15 km) and widening in the south (about 35 km). Considering the morphological characteristics of the PRE's shoreline, blunt-angled trumpet-shaped estuaries are generally thought to be less conducive to the formation of plume bulges. However, SAR imagery revealed a supercritical plume front in the southwest of the LC in the PRE, likely to be a plume bulge [29]. Subsequent numerical simulation studies and simultaneous observations by multiple vessels have confirmed the existence of the plume bulge in the PRE, and the effects of topography, wind, tides, and river discharge on the plume bulge have been discussed [21–25,29,30]. Based on the classification by salinity according to Simpsons et al. [31], these studies categorize the PRE plume into two types: surface-advected plume and tidal plume, utilizing the method of standardized analysis. The surface-advected plume is strongly stratified with low salinity, flowing out along the west coast. The tidal plume flowing from the LC, characterized by a higher degree of water mixing and higher salinity, is considered the main body forming the plume bulge [30].

However, the influence of PRE's river discharge on plume bulge formation remains uncertain. The results obtained through numerical experimental simulations are not the same as those obtained from the analysis of observation data. A number of numerical simulation experiments under different river discharge conditions suggest that the formation of plume bulges is not sensitive to the changes in river discharge. The direct contribution of river discharge to ebbing tide currents is not significant, but the cumulative enhancement of diluted water accelerates the formation of plume bulges [27]. The plume bulge in PRE formed under most of the discharge rate conditions, except the discharge rate of 3858 m³/s [23]. However, the investigations through observation data have shown that variations in river discharge significantly impact the formation of plume bulges. Plume bulge existed under a discharge condition of 23,440 m³/s in flood season, but disappeared at a discharge condition of 11,148 m³/s in dry season [30]. These uncertainties indicate that understanding the impact mechanisms of PRE's river discharge variations on plume bulge formation is still incomplete, further in-depth physical mechanism research is needed.

In this study, numerical experiments on the response of plume bulge to river discharge changes are carried out based on the validated FVCOM model, and the important role of river discharge in the formation mechanism of plume bulge is revealed from the perspectives of plume mixing and plume flow through standardized analysis and momentum balance analysis. This study is arranged as follows: Section 2 provides an introduction to the study area, followed by a description of the observed data and methodology in Section 3. The analysis of the numerical experiments results is presented in Section 4. The discussions of the physical mechanisms underlying the response of the plume bulge to changes in river discharge in the PRE are given in Section 5. Finally, the conclusions are in Section 6.

2. Study Area

The PRE features a geomorphology with three shoals and two channels; the depth of the eastern channel is 10 m, while the western channel, known as LC, serves as the main channel with a maximum depth of up to 20 m. The depths in other areas are generally less than 10 m [25]. The annual river discharge volume of the Pearl River exceeds 338 billion m³, with the average river discharge during the flood season from April to September nearing 20,000 m³/s, accounting for 80% of the annual total. The dry season from October to March of the following year sees river discharge less than 5000 m³/s. The highest historical flood peak in the Pearl River occurred in June 2005, when the combined discharge at the Gaoyao, Shijiao, and Boluo stations reached 75,400 m³/s [32]. The Pearl River primarily enters the SCS through eight estuary gates: Humen, Jiaomen, Hongqili, Hengmen, Modaomen,

Jitimen, Hutiaomen, and Yammen, with the water from the four eastern gates (Humen, Jiaomen, Hongqili, and Hengmen) constituting 60% of the total river discharge of the PRE.

The climate characteristics of the PRE region are primarily influenced by monsoons. The flood season is dominated by mild and moist southwest monsoons with lower wind speed, generally less than 6 m/s. The dry season features lower temperatures and reduced rainfall. Influenced by the East Asian monsoon, cold and dry strong northeast winds prevail, with an average wind speed of about 6–10 m/s.

The tidal regime near the PRE is predominantly semidiurnal, exhibiting significant diurnal inequality. The primary semidiurnal constituent is M_2 , followed by the diurnal constituents K_1 and O_1 [33]. Each lunar day features two high and two low tides, with unequal tidal ranges between successive tides and differing durations of flood and ebbing.

According to satellite observations and multi-vessel synchronous observations, the region where the plume bulge occurs is located southeast of the Dawanshan Islands [29,30]. Hence, Sections A and B have been selected as the two main cross-plume sections, used for analyzing the horizontal and vertical distribution of the surface-advected plume and tidal plume (Figure 1).

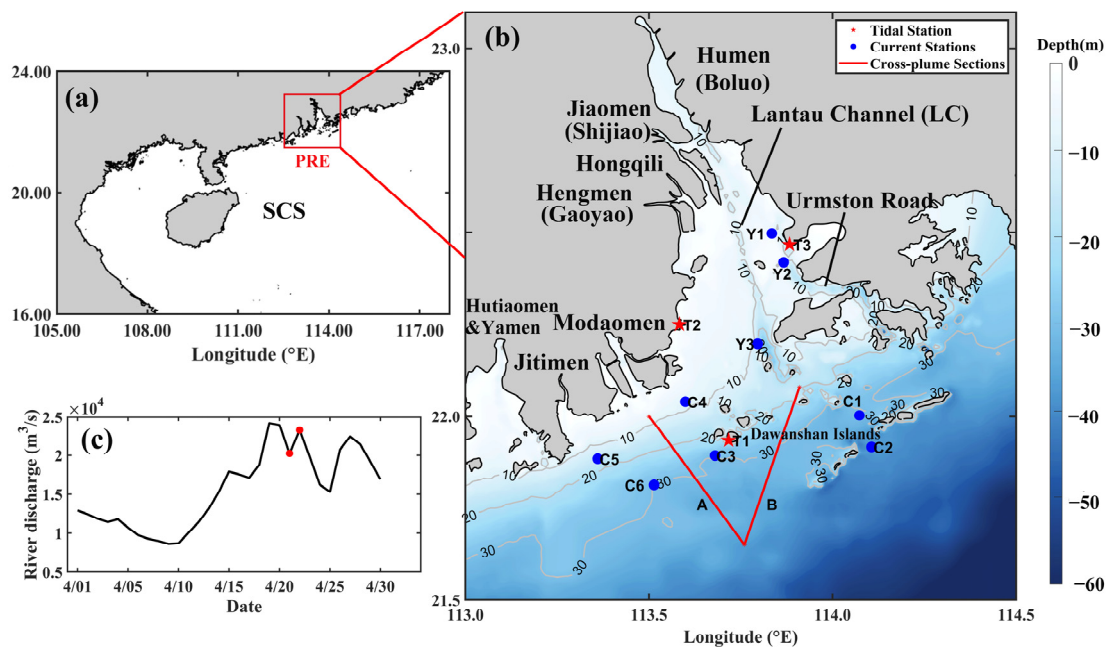


Figure 1. (a) Map of South China Sea (SCS). (b) Depth and the locations of stations of the Pearl River Estuary (PRE). The blue dots represent the locations of current stations. The red stars represent the tidal stations. The cross-plume sections in Section 4.4.2 are denoted by red segments. (c) River discharge of PRE in April 2019. The red points represent 2 and 23 April 2019.

3. Materials and Methods

3.1. Observation Data

The data from multiple synchronous multi-vessel observations were conducted at the PRE in 2019 for model validation, with the station locations shown in Figure 1. Tidal data were collected from Dawanshan, Zhuhai, and Chiwan long-term tidal stations (T1–T3, respectively) for 30 days in April 2019 with a time resolution of 1 h, which coincides with the observation time of current data. The current data were collected from three stations (Y1–Y3) near the LC during a mesotide to spring tide period (17–18 April 2019) and six stations (C1–C6) during another spring tide period (22–23 April 2019), with observations lasting over 25 h at a time resolution of 1 h, and vertically divided into three layers (0.5 m below the surface, mid-water at 0.6 H, and 0.5 m above the seabed). Most current-layer data were obtained using Seaguard RCM current meters, except for mid and bottom-layer data at station Y2, which were measured using a Nortek Aquadopp profiler ADCP (600 kHz), and

at stations C2 and C6, which were measured using a RDI WHS ADCP (600 kHz). Hourly salinity data were collected using SeaBird 37SM plus CTDs with an accuracy of 0.002. The observation stations were C1–C6, with observation times and intervals synchronized with the current data. River discharge data were obtained from daily river flow measurements at Gaoyao, Shijiao, and Boluo stations published by the Ministry of Transport's Pearl River Maritime Administration. The average daily river discharge of the Pearl River on 22–23 April reached 23,440 m³/s, far exceeding the average flood season discharge in 2019 (15,413 m³/s). Bathymetric data were derived from nautical charts measured and published by the Hydrographic Office of the Chinese Navy for the years 2009, 2011, 2013, 2014, and 2016. Shoreline data were extracted from Landsat-8 imagery (developed by NASA and the U.S. Geological Survey (USGS) in cooperation).

3.2. Model Configuration

The FVCOM [34] is used in this study. While in the vertical direction, it utilizes a σ -coordinate transformation.

Continuity equation:

$$\frac{\partial \zeta}{\partial t} + \frac{\partial Du}{\partial x} + \frac{\partial Dv}{\partial y} + \frac{\partial \omega}{\partial \sigma} = 0 \quad (1)$$

Momentum equation:

$$\begin{aligned} \frac{\partial uD}{\partial t} + \frac{\partial u^2D}{\partial x} + \frac{\partial uvD}{\partial y} + \frac{\partial u\omega}{\partial \sigma} - f v D = -gD \frac{\partial \zeta}{\partial x} \\ - \frac{gD}{\rho_0} \left[\frac{\partial}{\partial x} \left(D \int_{\sigma}^0 \rho d\sigma' \right) + \sigma \rho \frac{\partial D}{\partial x} \right] + \frac{1}{D} \frac{\partial}{\partial \sigma} \left(K_m \frac{\partial u}{\partial \sigma} \right) + DF_x \end{aligned} \quad (2)$$

$$\begin{aligned} \frac{\partial vD}{\partial t} + \frac{\partial uvD}{\partial x} + \frac{\partial v^2D}{\partial y} + \frac{\partial v\omega}{\partial \sigma} + f u D = -gD \frac{\partial \zeta}{\partial y} \\ - \frac{gD}{\rho_0} \left[\frac{\partial}{\partial y} \left(D \int_{\sigma}^0 \rho d\sigma' \right) + \sigma \rho \frac{\partial D}{\partial y} \right] + \frac{1}{D} \frac{\partial}{\partial \sigma} \left(K_m \frac{\partial v}{\partial \sigma} \right) + DF_y \end{aligned} \quad (3)$$

$$\frac{\partial TD}{\partial t} + \frac{\partial TuD}{\partial x} + \frac{\partial TvD}{\partial y} + \frac{\partial T\omega}{\partial \sigma} = \frac{1}{D} \frac{\partial}{\partial \sigma} \left(K_h \frac{\partial T}{\partial \sigma} \right) + D\hat{H} + DF_T \quad (4)$$

$$\frac{\partial SD}{\partial t} + \frac{\partial SuD}{\partial x} + \frac{\partial SvD}{\partial y} + \frac{\partial S\omega}{\partial \sigma} = \frac{1}{D} \frac{\partial}{\partial \sigma} \left(K_h \frac{\partial S}{\partial \sigma} \right) + DF_S \quad (5)$$

$$\rho = \rho(T, S) \quad (6)$$

where x , y , and z are the east, north, and vertical axes in the Cartesian coordinate system; u , v , and w are the x , y , and z velocity components; T is the temperature; S is the salinity; ρ is the density; P is the pressure; f is the Coriolis parameter; g is the gravitational acceleration; K_m is the vertical eddy viscosity coefficient; and K_h is the thermal vertical eddy diffusion coefficient. F_u , F_y , F_T , and F_S represent the horizontal momentum, thermal, and salt diffusion terms.

The domain of the model extends from 20.6–23.1° N, 112.25–115° E (Figure 2). The plume bulge occurs southwest of Dawanshan Island, which is at a relatively long distance (more than 100 km) from the modeled open boundary. For the PRE, such an open boundary is far enough away that the plume bulge is not constrained by the open boundary conditions [35]. The number of mesh nodes and triangles is 65,203 and 125,322, respectively. The horizontal mesh resolution of the open boundary of the control domain is 5000 m, while the horizontal mesh resolution of the PRE area reaches a minimum of 100 m. The model is divided into 20 σ -layers vertically (the water depth in PRE is 10–30 m). The number of CPUs for parallelization in this study is 144, the external time step is 3.0 s, internal time step is 7.5 s. The horizontal diffusion scheme uses the Smagorinsky eddy parameterization method [36], while the vertical diffusion scheme uses the Mellor and Yamada level 2.5 turbulent closure model [37].

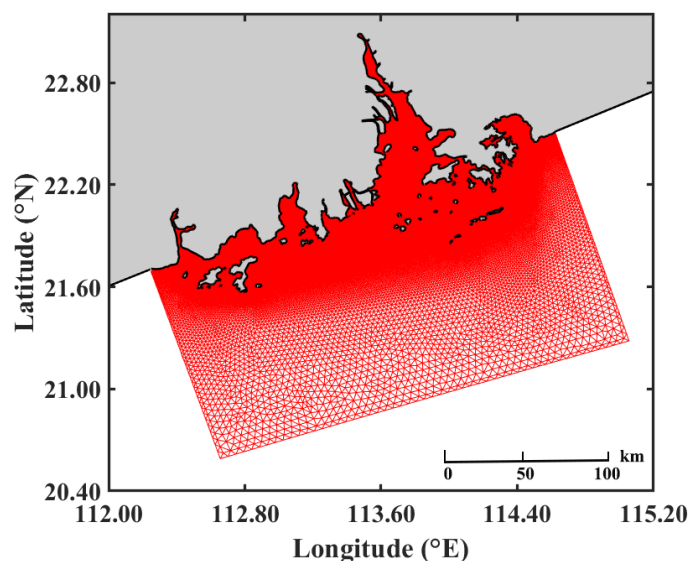


Figure 2. Domain area and computational mesh of the model. The distances of the study area from the eastern, southern, and western open boundaries are 109, 102, and 154 km, respectively.

The open boundaries of the model are driven by tidal level, current velocity, temperature, and salinity. The input data for low-frequency tidal level, low-frequency current, temperature, and salinity come from HYCOM reanalysis data (The HYbrid Coordinate Ocean Model and the Navy Coupled Ocean Data Assimilation, <http://hycom.org/dataserver/glb-reanalysis>, accessed on 1 September 2023) with a spatial resolution of $1/12^\circ$ by $1/12^\circ$ and a temporal resolution of 1 h [38,39]. To ensure the accuracy of model results, the data of high-frequency currents and tidal levels are added to the basic of low-frequency currents and tidal levels. The tidal dataset used for harmonic analysis is the TPXO9 dataset released by Oregon State University (<http://volkov.oce.orst.edu/tides/>, accessed on 1 September 2023), which includes the harmonic constants for four semidiurnal components (M_2 , S_2 , N_2 , and K_2) and four diurnal components (K_1 , O_1 , P_1 , and Q_1) [40]. For the surface forcing conditions, heat flux, precipitation, and atmospheric pressure data were collected from the ERA5 reanalysis data provided by the European Centre for Medium-Range Weather Forecasts (ECMWF), with a spatial resolution of 0.25° and a temporal resolution of 1 h (<http://www.remss.com/measurements/ccmp>, accessed on 1 October 2023) [41]. Due to the low observed wind speed during the study period, the wind field was turned off during the experiment (22–23 April 2019). Hourly wind field data for the remaining time were collected from the CFSR reanalysis dataset produced by the National Centers for Environmental Prediction (NCEP), with a spatial resolution of 0.25° and a temporal resolution of 1 h (download link: <http://hycom.org/dataserver/ncep-cfsr>, accessed on 1 September 2023) [42].

3.3. Model Validation

Two indicators are used to quantify the model's tidal level and current validation: Skill Score (SS) [43] and Correlation Coefficient (CC) [44]. Due to the influence of sea-land breezes and ship movements, the observation data of surface current velocity are not particularly accurate, so the current velocity has been processed through vertical averaging. According to the validation results of tidal levels and currents (Figure 3), semidiurnal tides and weaker diurnal tides dominate the PRE area, showing a clear tidal asymmetry phenomenon. Overall, the SSs and CCs for the tidal stations and current stations are high, indicating reliable simulation results for both tidal levels and currents.

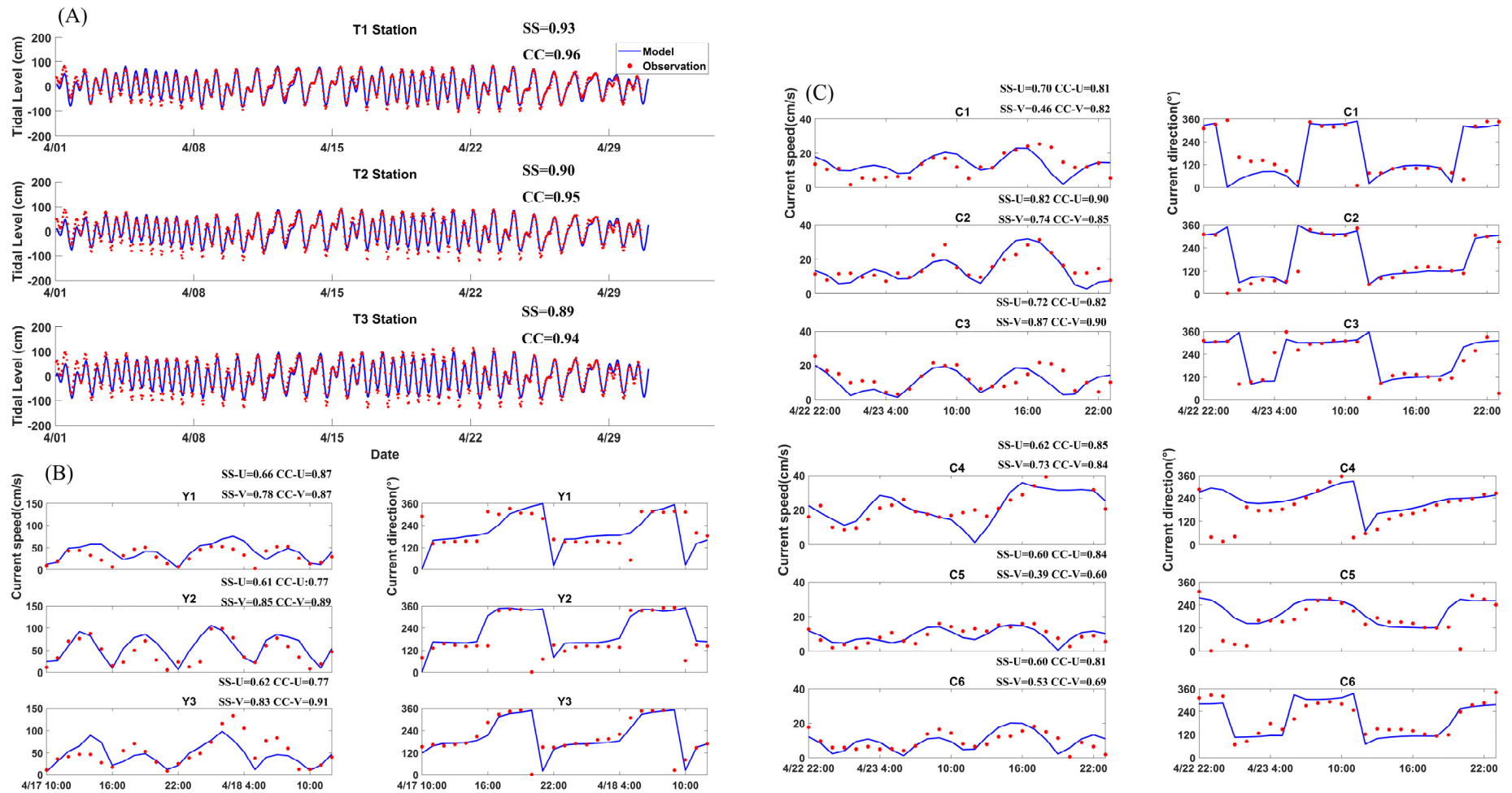


Figure 3. Comparison between observation data and model data. Blue lines are model data and red dots are observations. (A) Tidal stations; (B) Current stations Y1–Y3; (C) Current Stations C1–C6.

Since plume and plume bulge primarily occur in the surface and subsurface layers of the sea, the large-scale salinity validation is used to intuitively reflect the salinity simulation situation in the study area (Figure 4a1,a2). The observed large-scale salinity distribution came from stations C1-C6, representing the time-averaged results within a spring tide cycle. The results show that the simulation results are good in the area where the plume bulge appears.

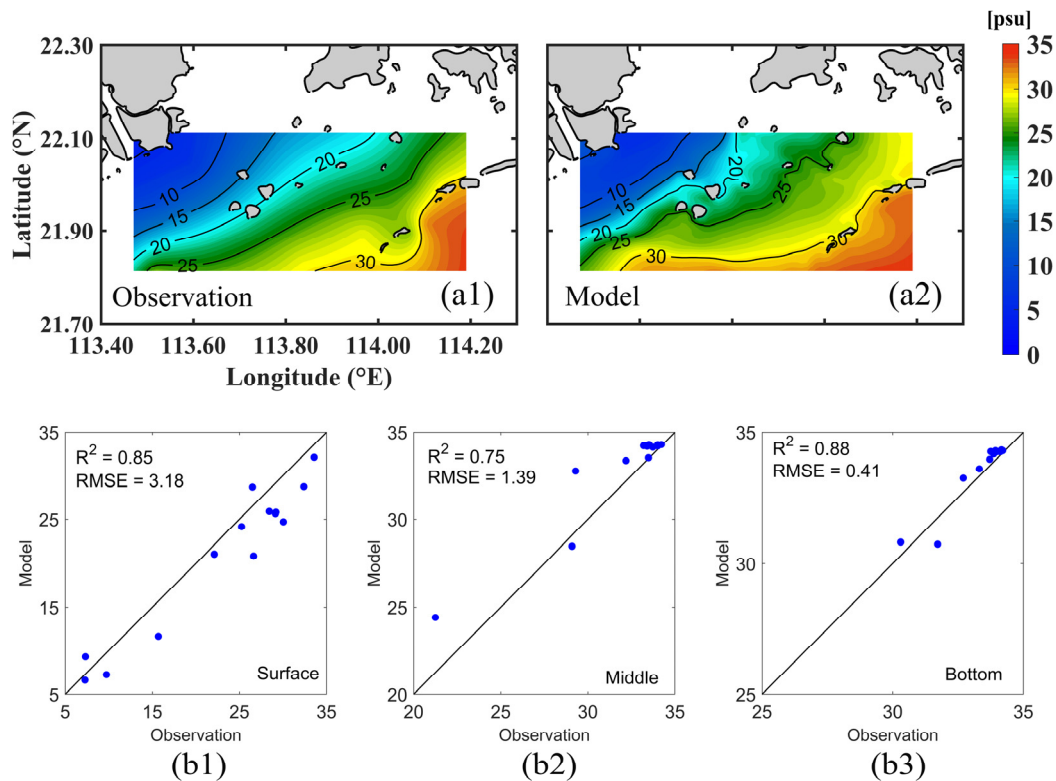


Figure 4. Large-scale verification of salinity in the surface layer. The (a1) is observation data and (a2) is model data. (b1–b3) are scatterplots of observation salinity and model salinity in each layer.

The coefficient of determination (R-squared, R^2) and the root mean squared error (RMSE) are used to quantify the results of the salinity validation of surface, middle, and bottom layers (Figure 4b1–b3) [44]. The data has been averaged over time. The results of R^2 in the middle layer are slightly underestimated compared to the results for the surface and bottom layers (Figure 4b2). A possible reason is that river discharge is released through selected elements acting as point sources, and the discharge must be released at every σ layer in FVCOM. Some stations located near some estuary mouths (e.g., C4 and C5) are in shallow waters, where the freshwater in the middle layer does not mix sufficiently with seawater after release, which may lead to this situation.

Overall, the results of R^2 and RMSE indicate that the model's simulation results in the study area match well with the observation data.

3.4. Model Setting

Five numerical experiments under different river discharge conditions are set (Table 1). According to observations by Li et al. [30], a river discharge of 23,340 m^3/s could significantly identify the variation of plume bulge in the spring tidal cycle. Therefore, the river discharge in Exp1 (Control) is set to 23,340 m^3/s . Exp2 has a river discharge set to 35,160 m^3/s ($1.5 \times$ Control). The river discharge set in Exp3 (11,720 m^3/s) corresponds to one of the numerical experiments by Pan et al. [23] and the observational analysis by Li et al. [30]. However, a plume bulge was observed in the numerical experiment but not in the observational analysis. Furthermore, Exp4 simulates an extreme river discharge

based on the historical peak river discharge in the Pearl River [32]. Finally, Exp 5 is set to simulate the average river discharge condition of the PRE during the dry season. Each set of experiments ran for a duration of four months to ensure the stability of the salinity simulation.

Table 1. Numerical experiment variable settings.

	Tide	River Discharge	Wind
Exp1 (Control)	Spring	23,440 m ³ /s	×
Exp2	Spring	35,160 m ³ /s (1.5× Control)	×
Exp3	Spring	11,720 m ³ /s (0.5× Control)	×
Exp4	Spring	70,320 m ³ /s (3× Control)	×
Exp5	Spring	5860 m ³ /s (0.25× Control)	×

3.5. Salinity Standardization Stratification Coefficient

The difference in potential energy (φ) is used in this study to quantify the production and disappearance of the stratification of the water. φ is the quantitative indicator of work where the unit volume of water is converted from stratification to a completely mixed condition (Jm⁻³). Higher values of φ represent stronger stratification of the water column, which is defined as follows [45]:

$$\varphi = \frac{1}{h} \int_{-h}^0 (\bar{\rho} - \rho_i) g z dz \quad (7)$$

where $\bar{\rho}$ is the density of the depth-averaged fluid, ρ_i is the density of the different water layers, z is the height above the bed, and h is the depth ($-h < z < 0$).

The water density ρ is defined by the following equation:

$$\rho = \rho_0(1 + \beta S_w) \quad (8)$$

where ρ_0 is the density of pure water, $\beta = 7.8 \times 10^{-4}$ is the haline contractivity, and S_w denotes the salinity of water.

The ratio of the energy required to mix the water body to the total potential energy is represented through Sr . Larger values of Sr represent stronger stratification of the water body. The calculation formula of Sr is [30]:

$$Sr = \frac{\varphi}{\bar{\varphi}} \times 100\% = \frac{\frac{1}{h} \int_{-h}^0 (\bar{\rho} - \rho_i) g z dz}{\frac{1}{2} \bar{\rho} g h} = \frac{\int_{-h}^0 (\bar{\rho} - \rho_i) g z dz}{\int_{-h}^0 \rho_i g z dz} \quad (9)$$

3.6. Amplitude of Tidal Salinity Variation

The effect of tides on salinity changes was determined by decomposing the surface, middle, and bottom salinities (S) into a tidally influenced fraction (S_T) and a residual fraction (S_R) through the salinity decomposition method. [23]:

$$S = S_T + S_R \quad (10)$$

Since the time-averaged value of S_T is 0 in a tidal period (25 h), so $\overline{S_T} = 0$ and $S_R = \bar{S}$. Thus, S_T can be derived as $S_T = S - \bar{S}$.

The amplitude of the tidal salinity variation (S_A) is defined as

$$S_A = \sqrt{2\overline{S_T^2}} \quad (11)$$

where S_A represents the amplitude of S_T .

Therefore, a higher value of S_A represents that the variation in salinity is predominantly driven by tides.

Based on the above materials and methods, the research structure of this research and the expected results are also shown (Figure 5).

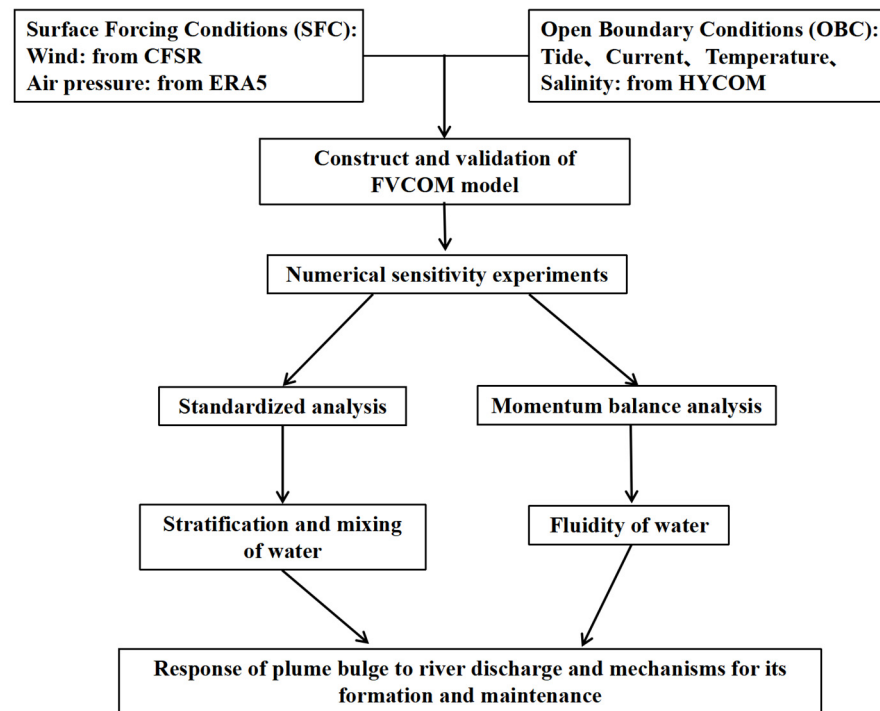


Figure 5. Diagram of research structure and expected results.

4. Results

4.1. Spatial and Temporal Evolution of the Plume Bulge in PRE

In order to contrast with previous observations and modeling results better [23,30], four typical tidal moments are chosen to analyze the temporal evolution (Figure 6a): Moments I–IV represent the lower high tide, higher lower tide, higher high tide, and lower low tide. For spatial characterization, the 25 isohaline contour line is considered to be the boundary of the plume bulge in PRE and can be used to analyze its spatial variability [30].

Exp1 (Control) demonstrates the distribution characteristics of the plume and plume bulge under conditions of strongly observed river discharge ($23,440 \text{ m}^3/\text{s}$) (Figure 6b1–b4,c1–c4,d1–d4). The freshwater with low salinity significantly influences the salinity distribution across the entire PRE, with average salinity gradually increasing from northwest to southeast. The diffusion range of freshwater is larger at the surface layer, while there is minimal outward diffusion of freshwater from the middle and bottom layers. The flow velocities in the mid and bottom layers are smaller compared to the surface layer (Figure 6c1–c4,d1–d4). The current velocity of specific areas increases due to the influence of ebbing at Moments II and IV (Figure 6c2,c4,d2,d4).

Due to the plume bulge occurring at the surface layer, the distribution of salinity and flow velocity at the surface layer is primarily analyzed. At Moment I (Figure 6b1), the volume of water on the west coast remains large, indicating that a large amount of freshwater is blocked by the flood tide from flowing along the western coast. Within the PRE, the current velocity in the region north of 22.3° N is relatively low. The 25psu isohaline is more significant on the southern side of the Dawanshan Islands, and the ‘arc’ shape of the plume bulge is clearly visible. At Moment II (Figure 6b2), due to the ebbing tide, the freshwater accumulated on the west coast is carried away from the shore, and the velocity of the current is reduced compared to Moment I. The tidal plume flowing out of LC forms an anticyclonic flow in the southwest of the Dawanshan Islands, making the 25 psu isohaline bulge structure clearer, which matches the morphology of the plume bulge observed by Li et al. [30]. At Moment III (Figure 6b3), the current velocity is low and stable

in the entire area due to the flood tide. The shape of the plume bulge is also more stable. At Moment IV (Figure 6b4), the average current velocity in the entire sea area increases, with the maximum current velocity of the seawater exiting LC reaching about 2 m/s, closely aligning with the flow field distribution characteristics analyzed by Li et al. [30] based on observational data. The volume of the surface-advected plume on the west coast increases, with the flow direction slightly deflecting towards the southwest. The plume bulge still exists; however, the anticyclonic flow generated by the tidal plume is not clear due to the influence of a strong ebbing tide.

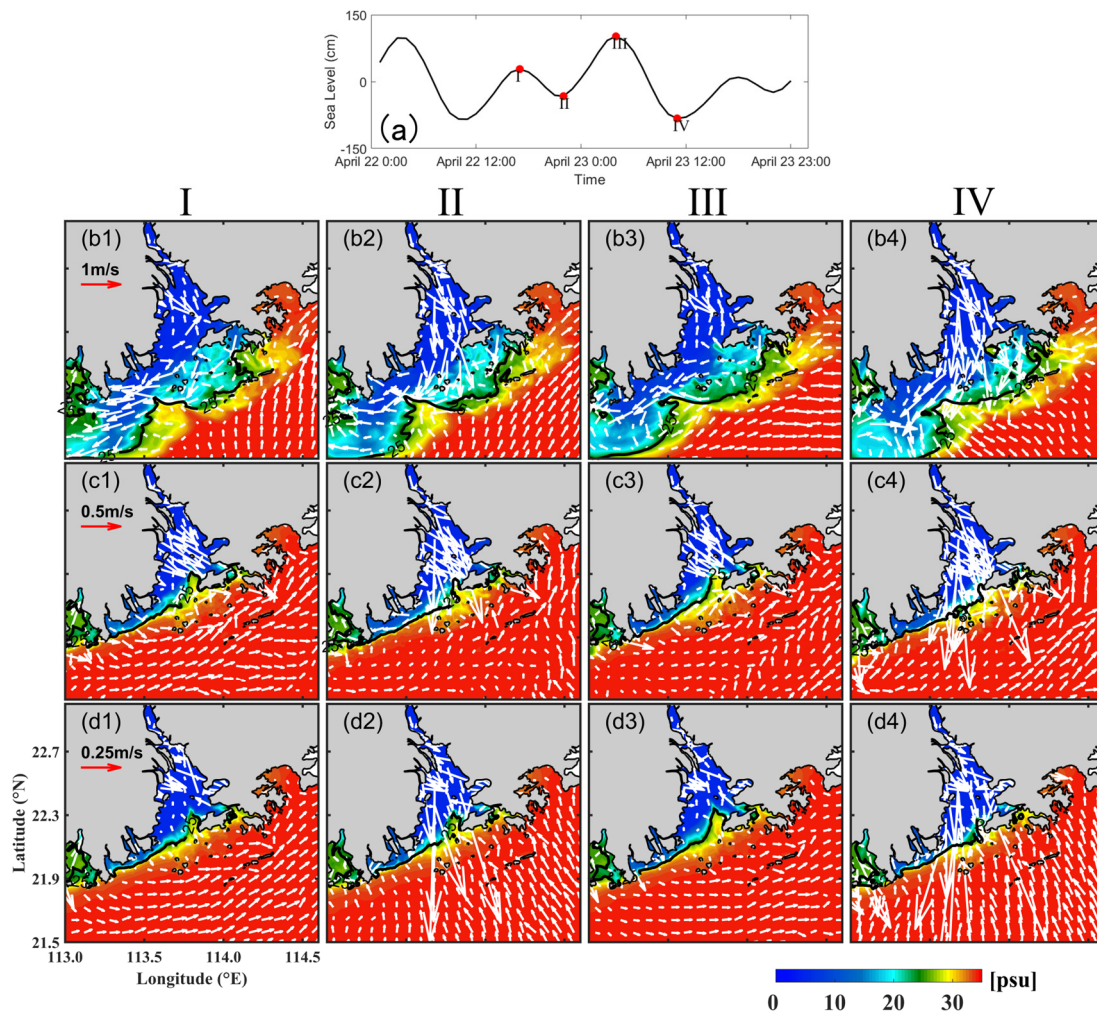


Figure 6. The top panel (a) shows the sea surface elevation of 22–23 April 2019 at T2 Station (the red star in Figure 1). Moments I–IV are represented by red points. (b1–b4,c1–c4,d1–d4) Salinity-current distribution for the surface layer, middle layer, and bottom layer, respectively; the color and white arrows represent the salinity field and current field, respectively.

4.2. Horizontal Distribution of the Plume Bulge in PRE after River Discharge Changes

The results of Exp2 (Figure 7b1–b4) indicate that as the river discharge increases, the current velocity of the entire current field increases, and the diffusion area of the plume expands. The volume of the surface-advected plume on the west coast increases, the anticyclonic flow formed by the tidal plume is clearer compared to Exp1, the plume bulge is more evident and its position moves southward, reaching up to 21.7° N. At Moment II (Figure 7b2), the increase in river discharge leads to a greater accumulation of freshwater within the bulge and a corresponding increase in the amount of freshwater carried out by the ebbing tide. The location of the anticyclonic flow in the southwestern part of the Dawanshan Islands is further southward and the current velocity is increased. At

Moments III and IV (Figure 7b3,b4), a cyclonic flow occurred near 113.3–113.5°E, resulting in the storage of some high-salinity seawater. The results of Exp3 (Figure 7c1–c4) show that when the river discharge decreased to half of that in Exp1 (11,720 m³/s), the overall salinity outside the PRE increased. The velocity and volume of the tidal plume significantly decreased, with freshwater with low salinity primarily flowing out along the western coast to form a surface-advected plume. The 25 isohaline contour line is located near the Dawanshan Islands, with no plume bulge formation. The result is consistent with the observations of Li et al. [30] but different from the model results of Pan et al. [23]. Under the extreme river discharge condition of Exp4 (Figure 7d1–d4), the salinity distribution outside the PRE remained essentially unchanged over time. The momentum of the freshwater sharply increased, with all the water exiting the estuary moving westward, as far south as 21.6° N. There is no plume bulge observed. Exp5 indicates that under average dry season river discharge conditions, current velocity is relatively low throughout the whole region (Figure 7e1–e4). The freshwater is essentially confined within the estuary and does not flow outward, a plume bulge is not formed.

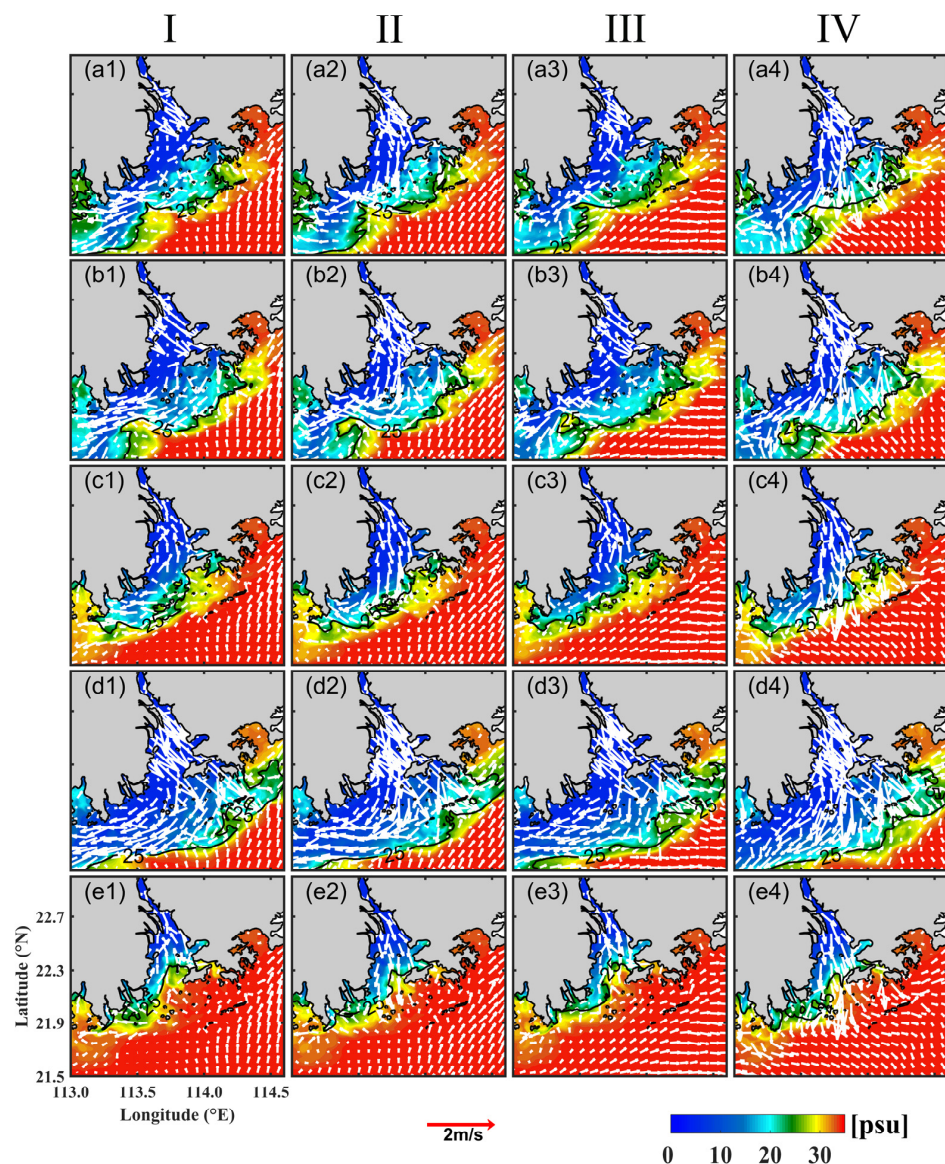


Figure 7. Salinity-current distributions of the surface layer of all experiments, (a1–a4,b1–b4,c1–c4, d1–d4,e1–e4) represent Exp1–Exp5, respectively; colors represent the salinity distribution and white arrows represent the current vectors.

4.3. Vertical Distribution of the Plume Bulge in PRE

In order to investigate the effect of river discharge on the vertical structure of the plume bulge, two cross-plume sections were selected for the study (Figure 1). Section A is approximately perpendicular to the topographic isobath and crosses the surface-advected plume distribution zone to the north and the plume bulge distribution zone to the south. Section B begins at the southern conjunction of section A and crosses the right distribution of the plume bulge, where the distribution of the tidal plume is also well observed.

In Section A, the results of Exp1 (Figure 8a1–a4) show a relatively stable vertical structure of the plume, with no significant changes within the tidal cycle. From the analysis of the horizontal distribution, the surface-advected plume is located west of 113.62° E. Salinity gradients mainly change in the nearshore area, especially in shallower waters where a halocline forms. The plume bulge begins to appear east of 113.62° E, and its thickness decreases with increasing distance from the shore, vanishing around 113.66° E. At Moments I and III (Figure 8a1,a3), freshwater mixes with high-salinity water brought by the flood tide, and the thickness of the bulge is only 2–3 m. At moments II and IV (Figure 8a2,a4), the bulge's thickness can increase up to 4 m due to the ebbing tide. The results of Exp2 (Figure 8b1–b4) indicate the volume of freshwater increases throughout the region as a river discharge increases. Halocline occurs at a deeper depth. The range of the plume bulge expands as far as 113.73° E. The thickness of the plume bulge at Moment IV reaches up to 7 m (Figure 8b4). While it remains around 5–6 m at other times. In Exp3 (Figure 8c1–c4), the volume of the nearshore surface-advected plume decreases. The vertical mixing driven by tidal dynamics becomes the dominant factor at other locations. This leads to a reduction in the internal salinity gradient of the plume. Furthermore, no plume bulge appears east of 113.62° E. The results of Exp4 (Figure 8d1–d4) under extreme river discharge conditions show that throughout the tidal cycle, a large amount of freshwater floats above the high-salinity seawater. However, based on the horizontal distribution (Figure 7d1–d4), the freshwater is a surface-advected plume rather than a tidal plume, and there is no plume bulge formation. In Exp5 (Figure 8e1–e4), under the conditions of average dry season river discharge, freshwater hardly diffuses to the location of Section A. The salinity of seawater throughout the region is relatively high (exceeding 30 psu) and remains essentially unchanged with tides.

In Section B, the tidal plume floats on the high-salinity seawater. The salinity of the tidal plume is higher than the surface-advected plume on the west coast, ranging between 20–25 psu, and there is no halocline. The plume bulge is visible from 113.82° E eastward, with a thickness of 2–3 m in Exp1 (Figure 8a1–a4). The distribution of the water column is relatively stable and salinity varies little with tides. In Exp2 (Figure 9b1–b4), the volume of surface freshwater increases. The plume bulge is visible from 113.78° E, with its range expanding compared to Exp1 and the thickness maintained at about 4 m. In Exp3 and Exp5 (Figure 9c1–c4,e1–e4), weaker river discharge prevents freshwater from continuing to expand southward, leading to the absence of a tidal plume and plume bulge along Section B. The salinity of the surface-floating freshwater is relatively high. The results of Exp4 under extreme river discharge conditions show that the volume of the plume is large, but a strongly mixed tidal plume does not occur (Figure 9d1–d4). The salinity of the freshwater is relatively low. Based on the horizontal distribution (Figure 7d1–d4), the freshwater is a surface-advected plume.

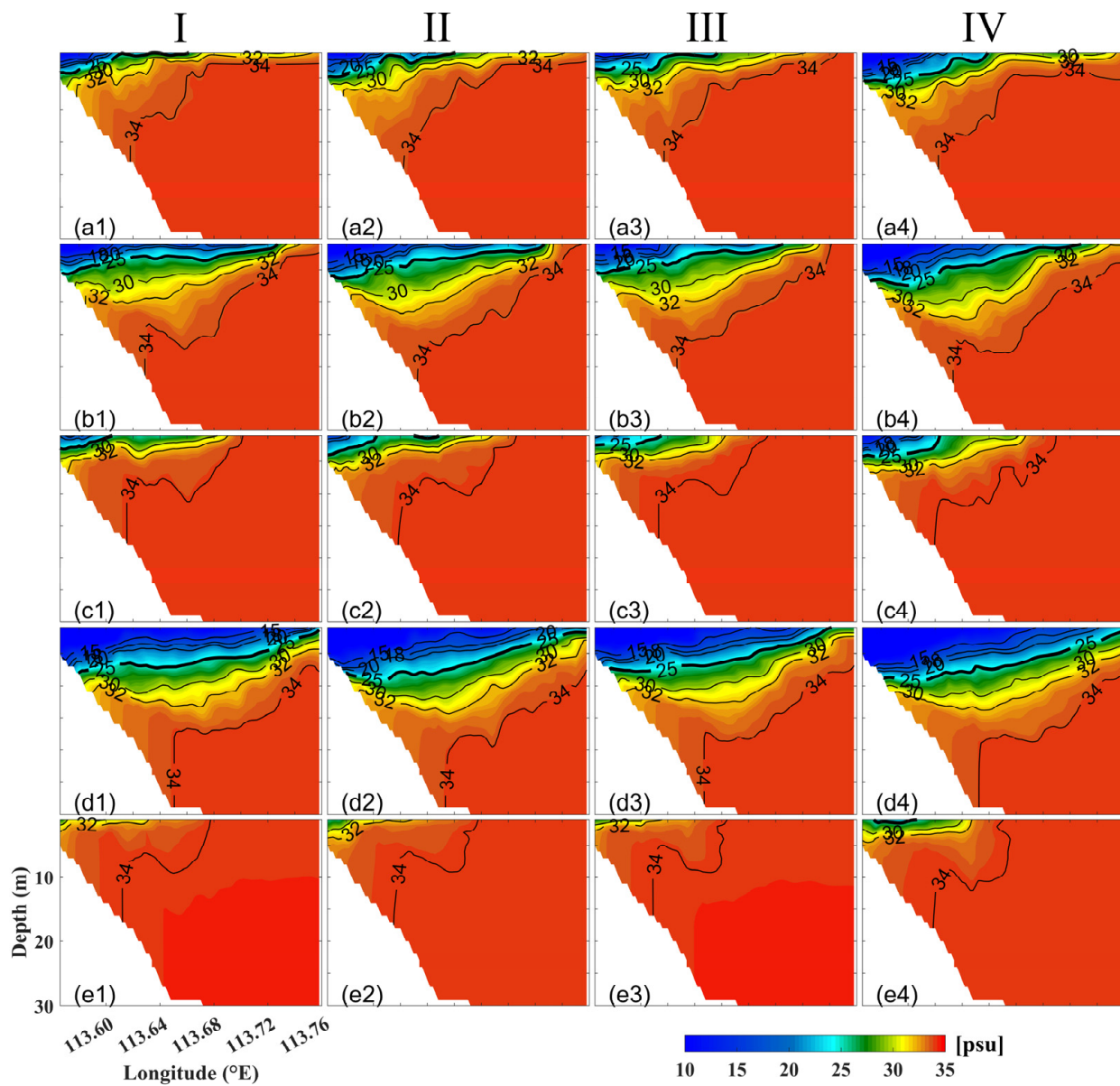


Figure 8. Vertical salinity distribution in Section A shown in Figure 1. Colors and contours represent the salinity, and vertical and horizontal coordinates indicate the water depth and longitude, respectively. (a1–a4,b1–b4,c1–c4,d1–d4,e1–e4) represent Exp1–Exp5, respectively.

4.4. Standardized Analysis

In this part, the effects of stratification (surface-advected plume) and mixing (tidal plume) on the bulge formation are investigated separately. Based on the analysis above, Exp5 demonstrates that the freshwater is blocked within the PRE and does not diffuse outside the estuary. Therefore, the mechanism analysis of Exp5 will not be discussed in the following parts.

4.4.1. Salinity Standardization Stratification Coefficient

According to the results, the changes in river discharge only affect the diffusion range and stratification of the surface-advected plume. The diffusion path will not be affected. The results of Exp1 (Figure 10a1–a4) show a strong stratification of the surface-advected plume flowing along the west coast. The maximum value of S_r can reach 1.0 near Modaomen and Jitimen. The freshwater mixes vertically with the higher salinity seawater at about 21.7° N and then dissipates. The results for moments II and IV indicate a reduction in S_r values

near Jitimen and Modaomen. The weakening of water stratification is caused by the ebbing tide carrying a significant amount of freshwater accumulated on the west coast away from the shore (Figure 10a2,a4).

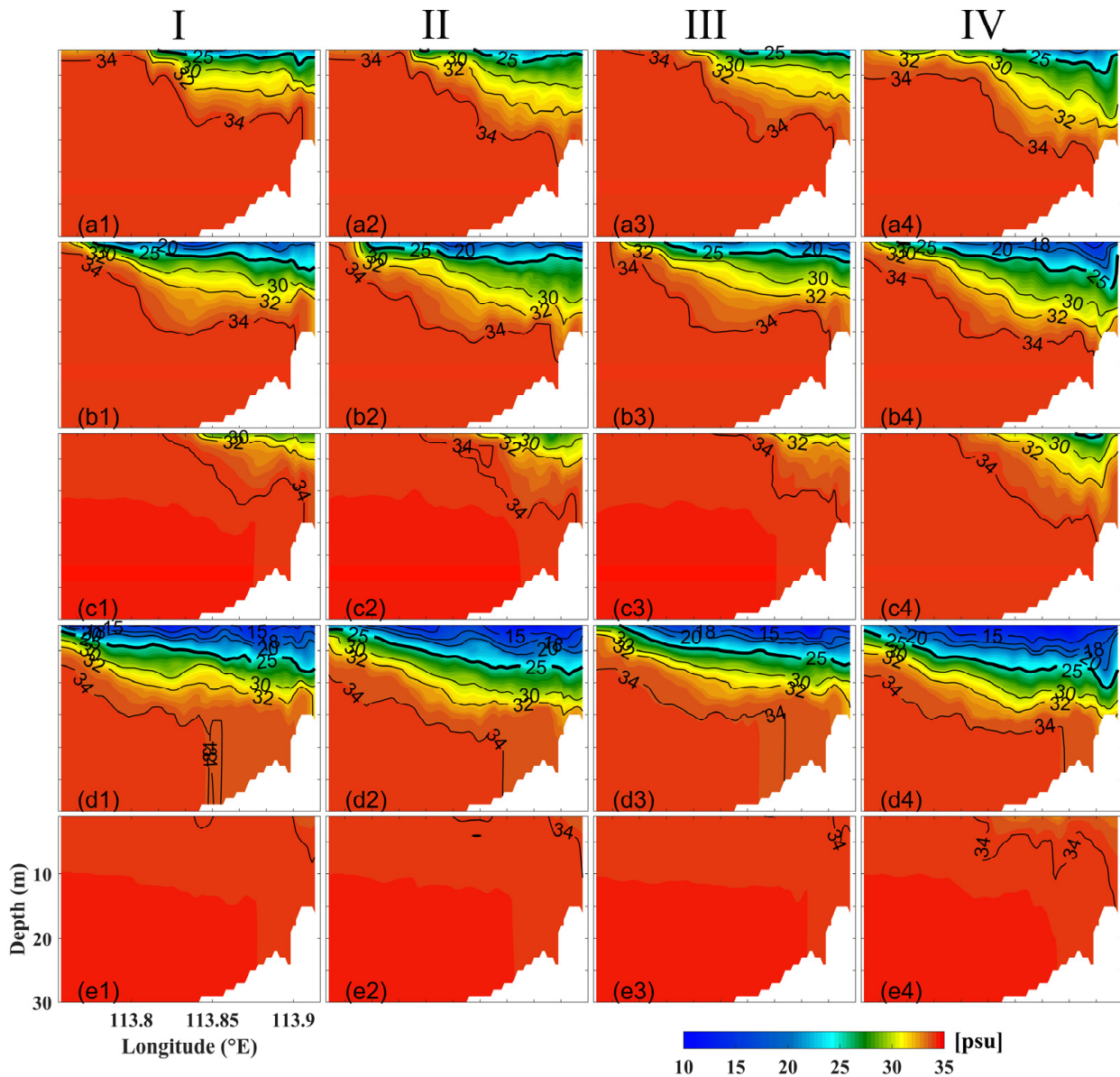


Figure 9. Vertical salinity distribution in Section B, shown in Figure 1, (a1–a4,b1–b4,c1–c4,d1–d4, e1–e4) represent Exp1–Exp5, respectively.

In Exp2 (Figure 10b1–b4), the overall distribution of S_r does not change significantly compared to Exp1, but the maximum value of S_r decreases. This is attributed to the increased river discharge enhancing the surface current velocity, which in turn weakens the stratification. In Exp3 (Figure 10c1–c4), the volume of the surface-advected plume decreases, but the degree of stratification remains strong. The results of Exp4 indicate that the stratification of the water body outside the PRE will be further weakened under extreme river discharge conditions.

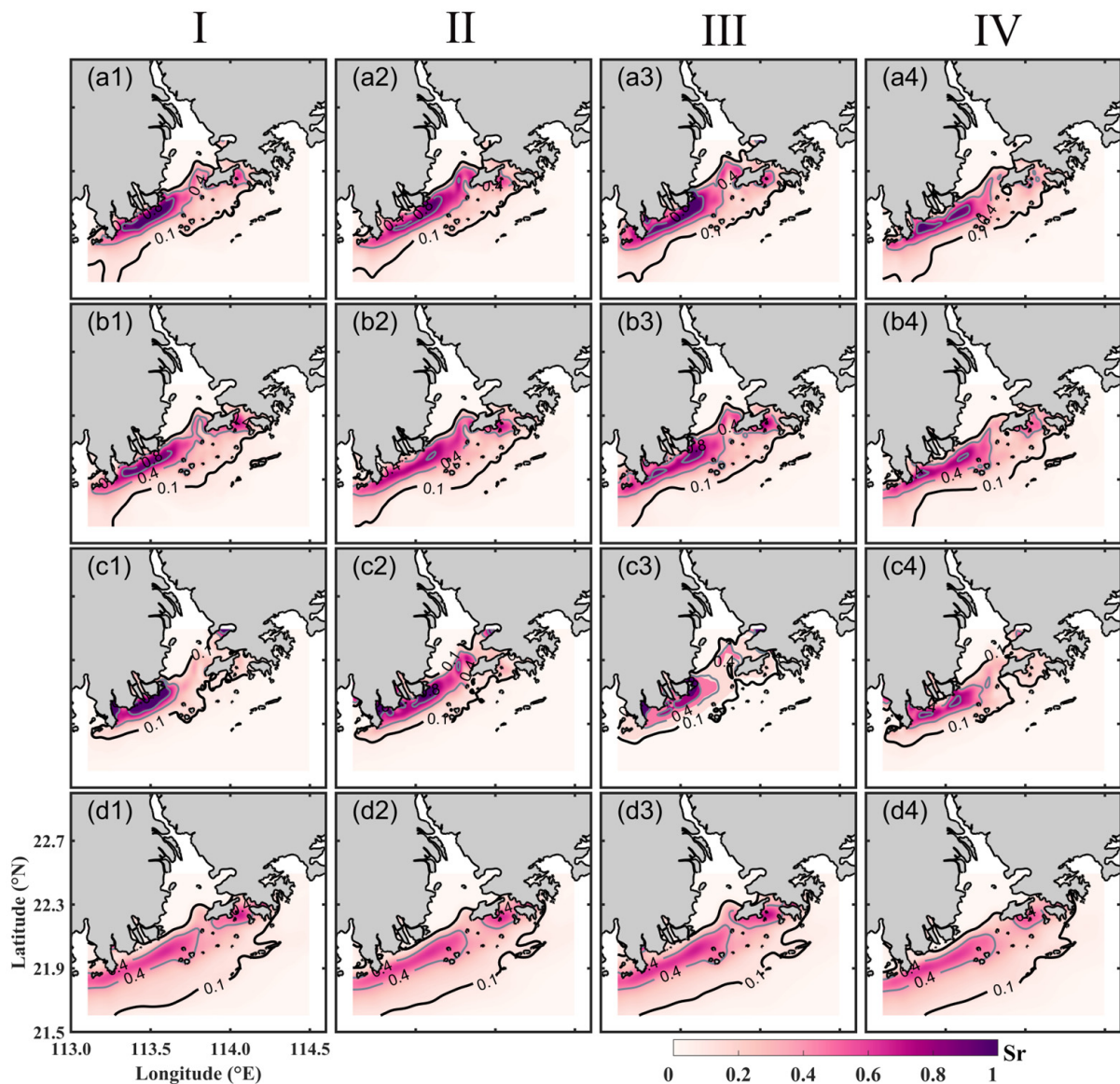


Figure 10. Distribution of S_r at Moments I–IV in PRE. (a1–a4,b1–b4,c1–c4,d1–d4) represent Exp1–4, respectively.

4.4.2. Amplitude of Tidal Salinity Variation

The distribution results of S_A in Exp1 demonstrate that tides significantly affect the variation of surface salinity at the estuary (Figure 11a1). High-value zones of S_A occur on the southwest side of the Dawanshan Islands, reaching up to 9. The location of the high-value area coincides with the area of the plume bulge and tidal plume. This indicates the dominant role of tidal plume in the formation of the plume bulge. The absence of tidal plumes at the same locations in the middle and surface layers (Figure 11a2,a3) might be due to the weakening of tidal mixing with increasing depth.

Exp2 (Figure 11b1–b3) indicates that the tidal influence expands seaward with increased river discharge. The high-value area of S_A moves further southwest and the maximum value increases to 10. In Exp3 (Figure 11c1–c3), the high-value area of S_A is closer to the West Coast and is not significant. The reduction in river discharge weakens the mixing of freshwater with seawater, leading to a decrease in the volume of the tidal plume and resulting in lower values of S_A . Under extreme river discharge conditions (Figure 11d1–d3), the mixing effect of tides is relatively weak. Tidal influence on surface salinity is minimal, and a plume bulge is not formed.

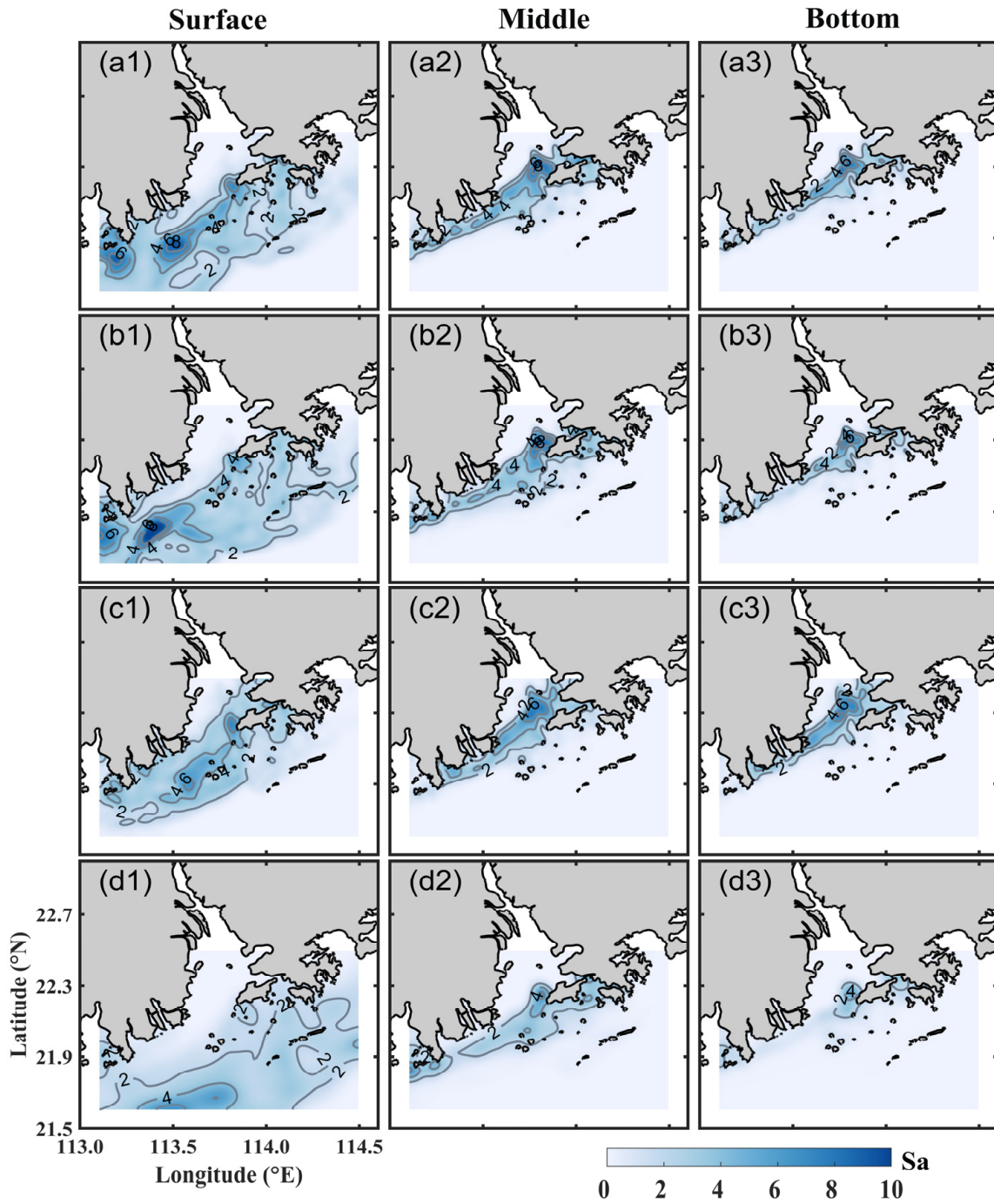


Figure 11. Distribution of S_A in PRE. Each column from left to right represents the surface, middle, and bottom layers, respectively. (a1–a3,b1–b3,c1–c3,d1–d3) represent Exp1–4, respectively.

4.5. Momentum Balance Analysis

To investigate the physical mechanisms behind the response of plume and plume bulge to river discharge, we conducted a momentum balance analysis of the surface layer in the study area. The results of the momentum balance have been time-averaged over 25 h to eliminate the effects of tidal oscillations. The equation for momentum diagnostics is as follows:

$$\underbrace{\frac{\partial u}{\partial t}}_{PAR} + \underbrace{u \frac{\partial u}{\partial x} + v \frac{\partial u}{\partial y} + w \frac{\partial u}{\partial z} - fv}_{HADV} + \underbrace{\frac{1}{\rho} \frac{\partial p}{\partial x}}_{COR} - \underbrace{\frac{\partial}{\partial x} \left(Ah \frac{\partial u}{\partial x} \right) - \frac{\partial}{\partial y} \left(Ah \frac{\partial u}{\partial y} \right)}_{HDIF} - \underbrace{\frac{\partial}{\partial z} \left(Az \frac{\partial u}{\partial z} \right)}_{VDIF} = 0 \tag{12}$$

$$\underbrace{\frac{\partial v}{\partial t}}_{PAR} + \underbrace{u \frac{\partial v}{\partial x} + v \frac{\partial v}{\partial y}}_{HADV} + \underbrace{w \frac{\partial v}{\partial z}}_{VADV} + \underbrace{fu}_{COR} + \underbrace{\frac{1}{\rho} \frac{\partial p}{\partial y}}_{PRSGRD} - \underbrace{\frac{\partial}{\partial x} \left(Ah \frac{\partial v}{\partial x} \right) - \frac{\partial}{\partial y} \left(Ah \frac{\partial v}{\partial y} \right)}_{HDIF} - \underbrace{\frac{\partial}{\partial z} \left(Az \frac{\partial v}{\partial z} \right)}_{VDIF} = 0 \quad (13)$$

where the abbreviation PAR represents localized partial derivatives of the velocities; HADV is the horizontal advection; VADV is the vertical advection; PRSGRD is the pressure gradient; COR is the Coriolis force; HADF is the horizontal diffusion; VDIF is the vertical diffusion. Because PAR, VADV, HDIF, and VDIF are relatively small compared to other terms, their effects are not considered in this study. Given that changes in salinity and water level significantly impact the variation of plume and plume bulge, the PRSGRD was divided into barotropic gradient (BARC) and baroclinic gradient (BART) for analysis.

Based on the model results, a momentum diagnostic analysis of the surface current field within the Exp1 study area was conducted (Figure 12a1–a4,b1–b4). The values of HADV are significantly larger primarily along the west and east coast within the PRE. The direction of HADV is complex in the PRE due to the complex topography (Figure 12a1,b1). This phenomenon occurs due to tidal rectification, which is the result of nonlinear interactions between tidal currents, topography, and riverine freshwater [46,47].

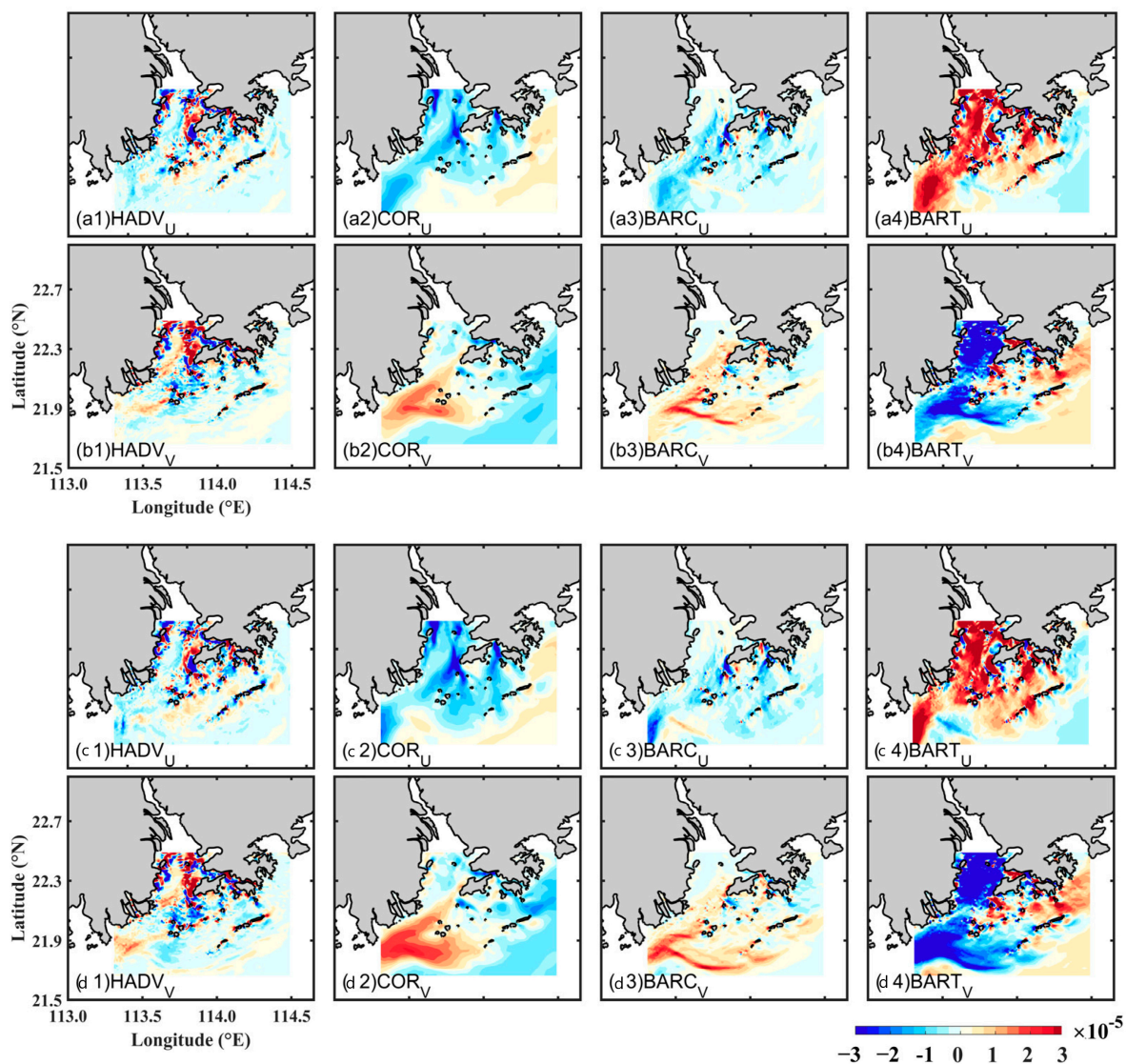


Figure 12. Distribution of the momentum balance terms for the surface layer in (a1–a4,b1–b4) Exp1, (c1–c4,d1–d4) Exp2. (a1–a4,c1–c4), and (b1–b4,d1–d4) represent U-direction and V-direction, respectively.

The Coriolis force plays a significant role across the entire area (Figure 12a2,b2). In the region of the west coast where the surface-advected plume exists, the direction of the Coriolis force is northwest. Near the LC on the eastern side of the Dawanshan Islands, the Coriolis force in the U-direction gradually changes from west to east as the latitude decreases. The Coriolis force in the V-direction gradually increases. This suggests that the tidal plume initially flows southward from the LC and gradually “turns” under the influence of the Coriolis force in the U-direction, resulting in anticyclonic flow near 21.9° N, 113.6–113.7° E.

The direction of the baroclinic gradient in the entire area is primarily northwest (Figure 12a3,b3). In the region from 21.7–21.9° N, 113.6–113.9° E, the direction of the baroclinic gradient in the U-direction turns eastward, forming an arc-shaped frontal zone, and a high-value area appears in the V-direction at the same location, with a maximum value reaching 2.5×10^{-5} . The location of the arc-shaped frontal zone is consistent with the location of the plume bulge analyzed previously. The direction of the baroclinic gradient force across the entire bulge region is northeast. The plume bulge formed by the anticyclonic flow stores a significant amount of freshwater, and the difference in salinity between the high-salinity seawater outside and the freshwater within the bulge enhances the baroclinic gradient force.

The primary direction of the barotropic gradient force outside the PRE is southeast (Figure 12a4,b4). In the bulge region, the direction of the baroclinic gradient force in the U-direction turns westward, and the overall direction of the barotropic gradient force across the bulge is southwest. This indicates that the water level within the plume bulge formed by the anticyclonic flow is higher than the surrounding areas, which in turn strengthens the barotropic gradient force.

The results of Exp2 indicate that the increase in river discharge did not change the dominant momentum terms in the entire study area (Figure 12c1–c4,d1–d4). The increase in river discharge leads to enhanced surface current velocity. Since the Coriolis force only changes the direction of the flow and not its magnitude, the Coriolis force in the U-direction changes from west to east at a more southerly location, thereby causing the tidal plume’s “turning” position to move southwest (Figure 12c1). Based on the distribution of the baroclinic and barotropic gradient terms, the location of the plume bulge also tends more toward the southwest (Figure 12c3,c4,d3,d4).

In Exp3, there is hardly any area where the Coriolis force in the U direction changes in PRE (Figure 13a2). This indicates that under the river discharge condition of 11,720 m³/s, the momentum is insufficient to maintain the tidal plume’s anticyclonic “turning”. The freshwater carried by tidal plumes is not enough to form strong salinity and water level differences with the high-salinity waters in the south. The arc-shaped frontal zone is not evident in the distribution of baroclinic and barotropic gradient terms (Figure 13a3,b3,a4,b4). Under extreme river discharge conditions, the Coriolis force is insufficient for the “turning” of the tidal plume due to the excessive surface current velocity. The plume bulge does not form. The current field outside the PRE is primarily dominated by the Coriolis force and the barotropic gradient force (Figure 13c2,d2,c4,d4).

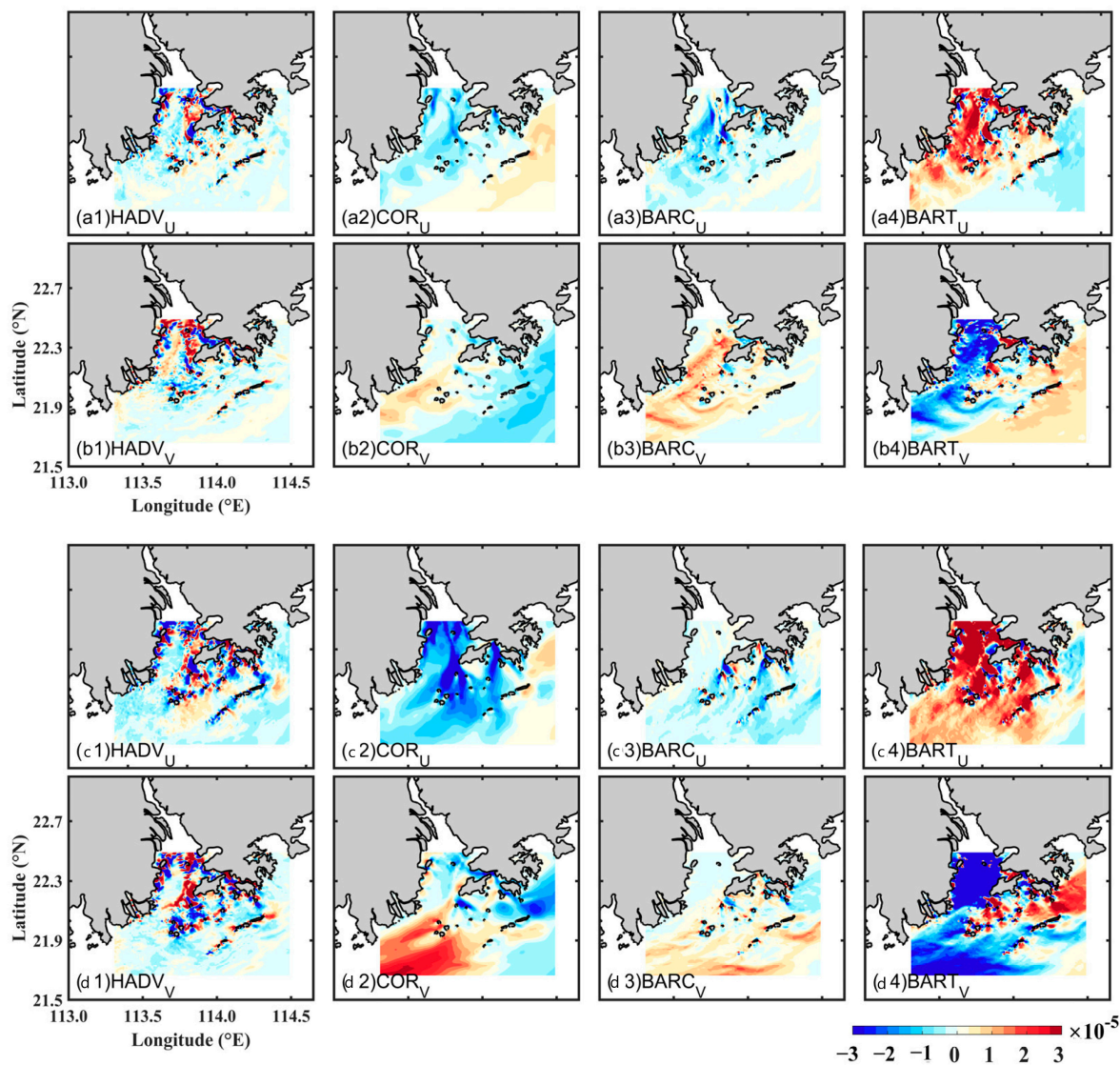


Figure 13. Distribution of the momentum balance terms for the surface layer in (a1–a4,b1–b4) Exp3, (c1–c4,d1–d4) Exp4., (a1–a4,c1–c4), and (b1–b4,d1–d4) represent U-direction and V-direction, respectively.

5. Discussion: The Mechanisms of Plume Bulge Formation and Maintenance

Under conditions of relatively high river discharge (Exp1 and Exp2), the volume of freshwater flowing out of the PRE is significant. Overall, the volume of the surface-advected plume is relatively small, whereas the volume of the tidal plume is relatively large. The salinity of the surface-advected plume flowing along the west coast is low (about 5–10 psu), with strong stratification, and a thickness of about 5 m. On the eastern side of the Dawanshan Islands, a large amount of freshwater can surge out from the LC, forming a tidal plume with relatively high salinity (about 25 psu) after intense mixing with tidal water, with a thickness of 3–4 m. A tidal plume is a prerequisite for the creation of a plume bulge.

The creation mechanism of the plume bulge can be divided into two stages. Stage 1 (formation): After the tidal plume flows out of the LC, the stronger river discharge enhances its momentum, leading to the formation of an anticyclonic flow on the southwest side of the Dawanshan Islands under the influence of the Coriolis force, thereby forming the plume bulge. Stage 2 (maintenance): The plume bulge stores a significant amount of freshwater. The difference in water level and salinity between the plume bulge and the surrounding water forms the barotropic and baroclinic gradient forces, which together with the Coriolis force maintain the stability of the plume bulge. However, under conditions of extreme river discharge (Exp4), the influence of water flow exceeds that of water stratification and

mixing. The plume bulge does not form. The current field outside the PRE is primarily dominated by the Coriolis force and the barotropic gradient force.

Under conditions of relatively low river discharge (Exp3 and Exp5), the volume of freshwater decreases. The volume of the surface-advected plume across the entire marine area becomes larger, and the volume of the tidal plume decreases as a result of the reduction in freshwater volume and the weakening of mixing. The momentum of flow is insufficient to maintain the tidal plume's anticyclonic "turning", and more of the tidal plume is confined to the west coast. Under these circumstances, the plume bulge does not form.

Based on the analysis of physical processes regarding water stratification, mixing, and flow dynamics presented above, the mechanisms of plume bulge formation and maintenance in the PRE have been well explained. The simulation results of this study by FVCOM are largely consistent with the two observational results of Li et al. [30], and the explanation of the mechanisms elucidates why such differences were observed in the two instances.

6. Conclusions

To investigate the spatio-temporal characteristics and response mechanisms of plume bulges under different river discharge conditions in the PRE, numerical experiments under five different river discharge conditions are conducted. By analyzing the horizontal and vertical distributions of the plume bulge, through standardized analysis and momentum balance analysis, the physical mechanisms of the plume bulge formation and its response to river discharge change were explored.

Under the influence of low salinity freshwater from river, the overall average salinity distribution in the PRE shows a trend of being lower in the northwest and higher in the southeast. Within a spring tidal cycle, salinity variations are influenced significantly by tidal changes. Ebbing tides facilitate the formation of plume bulges, but strong ebbing tides may be unfavorable for the formation of anticyclonic flow and plume bulges. Under strong river discharge conditions, the vertical structure of the plume changes little with the tidal cycle, and the structure of the plume bulge is clearer. Nearshore areas exhibit large vertical salinity gradients, while offshore areas are opposite. Under weak and extreme river discharge conditions, no plume bulge forms.

The west coast surface-advected plume is strongly stratified, expanding with increasing river discharge. A plume bulge is mainly generated by the anticyclonic flow formed by the tidal plume under the influence of the Coriolis force. Strong river discharge conditions (Exp1 and Exp2) enhance the mixing of low-salinity freshwater from river and tidal water, promoting the formation of tidal plumes. The combined action of barotropic and baroclinic gradient forces with the Coriolis force maintains the stability of the plume bulge. Under weak river discharge conditions (Exp3 and Exp5), the mixing of the water diminished. The momentum and flux of the tidal plume decrease, making it difficult for the plume bulge to form. Under extreme river discharge conditions (Exp4), the Coriolis force is insufficient for the "turning" of the tidal plume due to the excessive surface current velocity. The flow in the entire area is mainly balanced by the Coriolis force and barotropic gradient force.

In this study, the mechanism for the formation and maintenance of a mid-field plume bulge in PRE is obtained through standardized analysis and momentum balance analysis. This study is of great significance in terms of methodology and mechanism for studying the response mechanism of plume bulge to river discharge changes in other similar regions in the world.

Plume bulges can also be influenced by wind, tide conditions (spring and neap tide), and topography. However, this study exclusively focuses on the impacts of river discharge on plume bulges. The FVCOM model can simplify many complex physical processes into mathematical equations and involves some parameterization processes. However, all processes in the real-world ocean occur according to the fundamental principles of physics, chemistry, and biology, and are influenced by a variety of factors. In future numerical simulation studies, depending on the actual conditions, different wind fields

can be incorporated into the model, along with varying tidal conditions (spring and neap tide) and changes in topography. Their interacted physical mechanisms can be analyzed. Moreover, plume bulge has a significant impact on the biogeochemical environment of the PRE. An ecological module can be coupled with the existing FVCOM hydrodynamic model to explore the underlying mechanisms.

Author Contributions: Conceptualization, C.Z. and N.W.; resources, X.B.; methodology, N.W. and M.L.; funding acquisition, L.Z., D.S. and J.L.; visualization, C.Z. and H.Y.; writing—original draft, C.Z. and N.W.; writing—review and editing, N.W., Y.D. and H.Y.; model construction and validation, C.Z. and Y.C. All authors have read and agreed to the published version of the manuscript.

Funding: This study was funded by Key Laboratory of Ocean Space Resource Management Technology MNR (KF-2023-111), the National Natural Science Foundation of China (42076010, 41876088, U1706215), the Taishan Scholar Foundation of Shandong Province, China (tsqn202211056), the foundation of Guangdong Province Observation and Research Station for Coastal Upwelling Ecosystem (CUE202301) and Mauritius Marine Spatial Planning Research.

Data Availability Statement: Data will be made available on request.

Acknowledgments: C.Z. thanks X.L. to help in solving problems with the model runs. The authors thank to the anonymous reviewers for providing revisions. The calculation job is done through the High-performance Computer by Marine Big Data Center of Institute for Advanced Ocean Study of Ocean University of China.

Conflicts of Interest: The authors declare no conflict of interest.

References

1. Horner-Devine, A.R.; Hetland, R.D.; MacDonald, D.G. Mixing and Transport in Coastal River Plumes. *Annu. Rev. Fluid Mech.* **2015**, *47*, 569–594. [[CrossRef](#)]
2. Yankovsky, A.E.; Chapman, D.C. A Simple Theory for the Fate of Buoyant Coastal Discharges. *J. Phys. Oceanogr.* **1997**, *27*, 1386–1401. [[CrossRef](#)]
3. Garvine, R.W. A steady state model for buoyant surface plume hydrodynamics in coastal waters. *Tellus.* **1982**, *24*, 293–306. [[CrossRef](#)]
4. Lentz, S.J.; Helfrich, K.R. Buoyant gravity currents along a sloping bottom in a rotating fluid. *J. Fluid Mech.* **2002**, *464*, 251–278. [[CrossRef](#)]
5. Hetland, R.D. Relating river plume structure to vertical mixing. *J. Phys. Oceanogr.* **2005**, *35*, 1667–1688. [[CrossRef](#)]
6. Hetland, R.D. The effects of mixing and spreading on density in near-field river plumes. *Dyn. Atmos. Ocean.* **2010**, *49*, 37–53. [[CrossRef](#)]
7. McCabe, R.M.; MacCready, P.; Hickey, B.M. Ebb tide dynamics and spreading of a large river plume. *J. Phys. Oceanogr.* **2009**, *39*, 2839–2856. [[CrossRef](#)]
8. Lohan, M.C.; Bruland, K.W. Importance of vertical mixing for additional sources of nitrate and iron to surface waters of the Columbia River plume: Implications for biology. *Mar. Chem.* **2006**, *98*, 260–273. [[CrossRef](#)]
9. Bormans, M.; Garrett, C. A Simple Criterion for Gyre Formation by the Surface Outflow from a Strait, With Application to the Alboran Sea. *J. Geophys. Res.* **1989**, *94*, 12637–12644. [[CrossRef](#)]
10. Wiseman, J.W.J.; Garvine, R.W. Plumes and Coastal Currents Near Large River Mouths. *Estuaries* **1995**, *18*, 509–517. [[CrossRef](#)]
11. Yu, L.; Gan, J.; Dai, M.; Hui, C.R.; Lu, Z.; Li, D. Modeling the role of riverine organic matter in hypoxia formation within the coastal transition zone off the Pearl River Estuary. *Limnol. Oceanogr.* **2021**, *66*, 452–468. [[CrossRef](#)]
12. Li, D.; Gan, J.; Hui, C.; Yu, L.; Liu, Z.; Lu, Z.; Kao, S.J.; Dai, M. Spatiotemporal Development and Dissipation of Hypoxia Induced by Variable Wind-Driven Shelf Circulation Off the Pearl River Estuary: Observational and Modeling Studies. *J. Geophys. Res. Ocean.* **2021**, *126*. [[CrossRef](#)]
13. Masse, A.K.; Murthy, C.R. Analysis of the Niagara River Plume Dynamics. *J. Geophys. Res.* **1992**, *97*, 2403–2420. [[CrossRef](#)]
14. Chant, R.J.; Glenn, S.M.; Hunter, E.; Kohut, J.; Chen, R.F.; Houghton, R.W.; Bosch, J.; Schofield, O. Bulge Formation of a Buoyant River Outflow. *J. Geophys. Res. Ocean.* **2008**, *113*. [[CrossRef](#)]
15. Horner-Devine, A.R. The Bulge Circulation in the Columbia River Plume. *Cont. Shelf Res.* **2009**, *29*, 234–251. [[CrossRef](#)]
16. Horner-Devine, A.R.; Jay, D.A.; Orton, P.M.; Spahn, E.Y. A conceptual model of the strongly tidal Columbia River Plume. *J. Mar. Syst.* **2009**, *78*, 460–475. [[CrossRef](#)]
17. Rong, Z.; Li, M. Tidal effects on the bulge region of Changjiang River Plume. *Estuar. Coast Shelf Sci.* **2012**, *97*, 149–160. [[CrossRef](#)]
18. Münchow, A.; Garvine, R.W. Dynamical Properties of a Buoyancy-Driven Coastal Current. *J. Geophys. Res.* **1993**, *98*, 20063–20077. [[CrossRef](#)]

19. Simpson, J.H.; Bos, W.G.; Schirmer, F.; Souza, A.J.; Rippeth, T.P.; Jones, S.E.; Hydes, D. Periodic Stratification in the Rhine ROFI in the North Sea. *Oceanol. Acta* **1993**, *16*, 23–32.
20. Huq, P. The Role of Kelvin Number on Bulge Formation from Estuarine Buoyant Outflows. *Estuaries Coasts* **2009**, *32*, 709–719. [[CrossRef](#)]
21. Gu, Y.; Li, P.; Li, M. Numerical modeling and theoretical analysis of the existence of the Pearl River plume bulge. *Ocean Dyn.* **2019**, *69*, 1155–1163. [[CrossRef](#)]
22. Xia, M.; Xie, L.; Pietrafesa, L.J.; Whitney, M.M. The ideal response of a Gulf of Mexico estuary plume to wind forcing; Its connection with salt flux and a Lagrangian View. *J. Geophys. Res. Ocean.* **2011**, *116*. [[CrossRef](#)]
23. Pan, J.; Gu, Y.; Wang, D. Observations and numerical modeling of the Pearl River plume in summer season. *J. Geophys. Res. Ocean.* **2014**, *119*, 2480–2500. [[CrossRef](#)]
24. Pan, J.; Gu, Y. Cruise observation and numerical modeling of turbulent mixing in the Pearl River estuary in summer. *Cont. Shelf Res.* **2016**, *120*, 122–138. [[CrossRef](#)]
25. Liu, X.; Gu, Y.; Li, P.; Liu, Z.; Zhai, F.; Wu, K. A tidally dependent plume bulge at the Pearl River Estuary mouth. *Estuar. Coast Shelf Sci.* **2020**, *243*, 106867. [[CrossRef](#)]
26. Isobe, A. Ballooning of River-Plume Bulge and its Stabilization by Tidal Currents. *J. Phys. Oceanogr.* **2005**, *35*, 2337–2351. [[CrossRef](#)]
27. Garvine, R.W. The impact of model configuration in studies of buoyant coastal discharge. *J. Mar. Res.* **2001**, *59*, 193–225. [[CrossRef](#)]
28. Xia, M. *Cape Fear River Estuary Modeling System*; North Carolina State University: Raleigh, NC, USA, 2006.
29. Bai, P.; Gu, Y.; Luo, L.; Zhang, W.; Fan, K. Observation of the supercritical Pearl River plume front under the downwelling-favorable winds. *Sci. China Earth Sci.* **2015**, *58*, 2059–2066. [[CrossRef](#)]
30. Li, M.; Wang, N.; Li, G.; Song, D.; Gu, Y.; Bao, X.; Liu, S.; Zhang, L. Plume bulge observed in the Pearl River Estuary in summer: Spatiotemporal characteristics and influencing factors. *Estuar. Coast Shelf Sci.* **2023**, *282*, 108242. [[CrossRef](#)]
31. Simpson, J.H.; Allen, C.M.; Morris, N.C.G. Fronts on the continental shelf. *J. Geophys. Res. Ocean.* **1978**, *83*, 4607–4614. [[CrossRef](#)]
32. Yao, Z. The Characteristics and Warnings of the “June 2005” Storm Flood in the Pearl River Basin (in Chinese). *Exp. Water Res. Hydropower Inf.* **2008**, *29*, 68–74.
33. Zu, T.; Wang, D.; Gan, J.; Guan, W. On the role of wind and tide in generating variability of Pearl River plume during summer in a coupled wide estuary and shelf system. *J. Mar. Syst.* **2014**, *136*, 65–79. [[CrossRef](#)]
34. Chen, C.; Liu, H.; Beardsley, R.C. An Unstructured Grid, Finite-Volume, Three-Dimensional, Primitive Equations Ocean Model: Application to Coastal Ocean and Estuaries. *J. Atmos. Ocean. Technol.* **2003**, *20*, 159–186. [[CrossRef](#)]
35. Lin, S.; Liu, G.; Niu, J.; Wei, X.; Cai, S. Responses of hydrodynamics to changes in shoreline and bathymetry in the Pearl River Estuary, China. *Cont. Shelf Res.* **2021**, *229*, 104556. [[CrossRef](#)]
36. Smagorinsky, J. General Circulation Experiments with the Primitive Equations. *Mon. Weather Rev.* **1963**, *91*, 99–164. [[CrossRef](#)]
37. Mellor, G.L.; Yamada, T. Development of a Turbulence Closure Model for Geophysical Fluid Problems. *Rev. Geophys.* **1982**, *20*, 851–875. [[CrossRef](#)]
38. Bleck, R. An Oceanic General Circulation Model Framed in Hybrid Isopycnic-Cartesian Coordinates. *Ocean Model.* **2001**, *37*, 55–88. [[CrossRef](#)]
39. Chassignet, E.P.; Hurlburt, H.E.; Smedstad, O.M.; Halliwell, G.R.; Hogan, P.J.; Wallcraft, A.J.; Baraille, R.; Bleck, R. The Hycom (Hybrid Coordinate Ocean Model) Data Assimilative System. *J. Mar. Syst.* **2007**, *65*, 60–83. [[CrossRef](#)]
40. Egbert, G.D.; Erofeeva, S.Y. Efficient Inverse Modeling of Barotropic Ocean Tides. *J. Atmos. Ocean. Technol.* **2002**, *19*, 183–204. [[CrossRef](#)]
41. Hersbach, H.; Bell, B.; Berrisford, P.; Hirahara, S.; Horányi, A.; Muñoz Sabater, J.; Nicolas, J.; Peubey, C.; Radu, R.; Schepers, D.; et al. The Era5 Global Reanalysis. *Q. J. R. Meteorol. Soc.* **2020**, *146*, 1999–2049. [[CrossRef](#)]
42. Schneider, D.P.; Deser, C.; Fasullo, J.; Trenberth, K.E. Climate Data Guide Spurs Discovery and Understanding. *Eos Trans. Am. Geophys. Union.* **2013**, *94*, 121–122. [[CrossRef](#)]
43. Gao, G.D.; Wang, X.H.; Song, D.; Bao, X.; Yin, B.S.; Yang, D.Z.; Ding, Y.; Li, H.; Hou, F.; Ren, Z. Effects of Wave-Current Interactions on Suspended-Sediment Dynamics During Strong Wave Events in Jiaozhou Bay, Qingdao, China. *J. Phys. Oceanogr.* **2018**, *48*, 1053–1078. [[CrossRef](#)]
44. Zhi, H.; Wu, H.; Wu, J.; Zhang, W.; Wang, Y. River Plume Rooted on the Sea-Floor: Seasonal and Spring-Neap Variability of the Pearl River Plume Front. *Front. Mar. Sci.* **2022**, *9*, 791948. [[CrossRef](#)]
45. Simpson, J.H.; Bowers, D. Models of stratification and frontal movement in shelf seas. *Deep-Sea Res. Pt I* **1981**, *28A*, 727–738. [[CrossRef](#)]
46. Chen, C.; Beardsley, R.C. A Numerical Study of Stratified Tidal Rectification over Finite-Amplitude Banks. Part I: Symmetric Banks. *J. Phys. Oceanogr.* **1995**, *25*, 2090–2110. [[CrossRef](#)]
47. Ryan, H.F.; Noble, M.A.; Williams, E.A.; Schroeder, W.W.; Pennock, J.R.; Gelfenbaum, G. Tidal current shear in a broad, shallow, river-dominated estuary. *Cont. Shelf Res.* **1997**, *17*, 665–688. [[CrossRef](#)]

Disclaimer/Publisher’s Note: The statements, opinions and data contained in all publications are solely those of the individual author(s) and contributor(s) and not of MDPI and/or the editor(s). MDPI and/or the editor(s) disclaim responsibility for any injury to people or property resulting from any ideas, methods, instructions or products referred to in the content.